Molecular and Nano-engineering with iron, ruthenium and carbon: Hybrid structures for sensing

Geest, E.P. van

Chapter 3

Large-area thin films of the spin crossover complex [Fe(bapbpy)(NCS)$_2$] grown selectively on graphene

Spin-crossover (SCO) nanomaterials have raised technological interest for e.g. sensors and data storage devices, yet they require a readout platform as these materials are typically electrically insulating. We have developed a method to chemically grow large-area thin films from a solution of the SCO complex [Fe(bapbpy)(NCS)$_2$], with inherent selectivity for areas on silicon wafers that were coated with graphene. Extensive characterization of the films showed that the thin film material was chemically similar to single crystals of [Fe(bapbpy)(NCS)$_2$], albeit the film was amorphous and the iron in the thin films was typically more oxidized than in the single crystal material. Moreover, magnetic measurements suggested that the films were SCO-active. The thin films were also grown on graphene field effect transistors (GFETs), but so far these GFETs could not detect SCO events through electronic readout. Thin films based on the SCO complex [Fe(babpby)(NCS)$_2$] can thus be selectively grown from solution on graphene and GFETs, but whether spin switches can be electrically detected with these GFETs could not be demonstrated yet.

E.P. van Geest, P. van Deursen, L. Wu, N. Puthuval Prasad, T. de Haas, A. Rotaru, J.P. Hofmann, G.F. Schneider and S. Bonnet, manuscript in preparation.

3.1. Introduction

Molecular materials, or switching materials, have been recognized for their great potential in technological applications like sensing and data storage.[1] An important example is the class of spin crossover (SCO) materials, in which the switching of the spin state of individual molecules, triggered by external perturbations, results in the variations of for example the color and the magnetic susceptibility of the bulk material.[2, 3] However, a challenge in SCO research is to scale down the size of these materials, which is often required for their implementation in electronic devices.[4] Although small-scale structures, such as nanoparticles or thin films, can be obtained using common nanotechnology techniques, SCO materials are notoriously sensitive to minute changes in their chemical composition, environment, and morphology,[5] so that reducing the size of a 3D bulk material often comes with a trade-off; in the nanometer-size range, well-defined, complete spin crossover properties are often replaced for gradual and incomplete transitions, as was demonstrated with [Fe(pyrazine)[Pt(CN)$_4$] nanoparticles for example.[6]

Here, we report the results of our investigation whether it is possible to scale down one of the dimensions of the 3D single crystal of [Fe(bapbpy)(NCS)$_2$] (where bapbpy = N,N'-di(pyrid-2-yl)-2,2'-bipyridine-6,6'-diamine) while keeping the bulk SCO properties intact, and if thin films of this compound could be used to build graphene-based electronic sensors as we did previously with a 3D crystal, described in Chapter 2.[7] We used solution-based processes to grow the film, to not rely on technically complex methods like vacuum deposition.[8] One of the challenges with such methods is to retain the spin crossover properties of the bulk material. The bulk SCO properties of [Fe(bapbpy)(NCS)$_2$] crystals for instance changed dramatically upon DMF inclusion in the crystal lattice as the crystallization protocol was changed.[9] Wet thin film growth using DMF-containing solvent mixtures may hence produce thin films of different materials.

The nature of the surface on which the films grow is equally important. As has been demonstrated for example with calcite growth, surface modifications could alter the nucleation and crystal structure of materials grown on those surfaces, which could be used to tune the deposition process and properties of the deposited material.[10] Here, graphene was used as a substrate for the thin films, as the electronic properties of graphene (high electron mobility, high surface to

volume ratio, and low noise) are very suitable for sensing: graphene is sensitive to changes in the dipole moment of nearby molecules.[11] SCO molecules are known to undergo changes in their electric dipole when they switch their spin state from high spin to low spin;[7, 12] interfacing a SCO thin film with graphene may thus be useful to obtain electronic readout of the spin state of the SCO film, and hence to obtain a graphene-based sensor that is sensitive to its environment. In this work, we studied the wet growth of molecular thin films of [Fe(bapbpy)$(NCS)_2$] on graphene-functionalized silicon wafers, and investigated GFET devices based on these films.

3.2. Results and Discussion

3.2.1. Chemical growth of thin films

Thin films were grown by vapor-liquid diffusion of methanol into a DMF solution of the [Fe(bapbpy)$(NCS)_2$] complex in presence of a bare or graphene-coated silicon wafer. This methods differs from the classical method for growing 3D single crystals of [Fe(bapbpy)$(NCS)_2$], which consists of performing liquid-liquid diffusion of methanol in a DMF solution of the same complex in a plastic or glass tube.[13] Here, vapor-liquid diffusion experiments were performed in a cuvette, sitting in a snap-cap sample vial, in which the silicon wafer was placed beforehand, positioned vertically with respect to the DMF-methanol interface (see Figure 3.1A; for a photograph, see Figure S3.1). Degassed methanol was placed outside the cuvette, into the sample vial; the methanol vapor slowly diffused into the DMF solution, which drove film growth. Depending on the surface functionalization of the wafer, the thin film started to grow on the wafers after one or several days, as confirmed visually by the light interference effect typical for thin films grown on silicon wafers. The color of thin layer materials on wafers was strongly dependent on the thickness of the film, which provided optical contrast when neighboring layers were different in thickness.

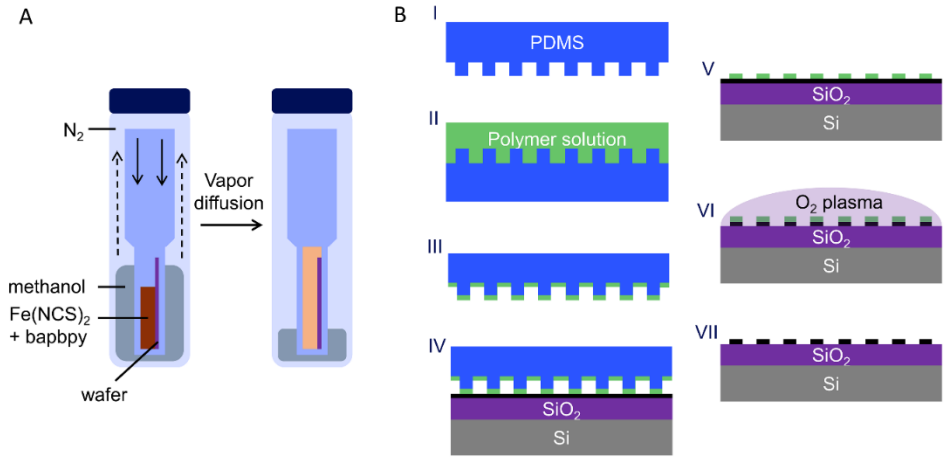

Figure 3.1: Thin film growth setup and graphene patterning. A) Schematic representation of the setup used for thin film growth via vapor diffusion of methanol. B) Schematic representation of μ-contact printing of polymer mask for graphene patterning. A stamp was created by PDMS casting on a patterned master (I), a droplet of polymer solution was placed on the stamp (II), and this solution was evenly distributed using spin coating (III). Next, the stamp was pressed on a silicon wafer, on which graphene (black line) was transferred before (IV), leaving the polymer at the surface where contact with the stamp was made (V). Oxygen plasma was used to remove unmasked graphene (VI) and the wafer was immersed in acetone to remove the mask and expose the patterned graphene (VII).

3.2.2. Thin films on graphene & patterned growth

To produce thin films of [Fe(bapbpy)(NCS)$_2$] on graphene, silicon wafers were first coated with centimeter-sized monolayer graphene, grown in-house on copper using a hot-wall chemical vapor deposition (CVD) oven, and transferred onto the wafer using poly(methyl methacrylate) (PMMA) assisted transfer. The molecular films were then grown over one to ten days as described above, which afforded centimeter-sized films with relatively uniform thicknesses, as observed qualitatively by their color (see Figure S3.2 for a film grown over five days). While methanol vapor diffusion yielded thin films, direct layering of liquid methanol on top of the complex solution on the other hand typically gave single crystals of the compound very quickly, already within one hour. Simply slowing down diffusion of methanol into the DMF solution of the complex thus had a large effect on the morphology of the material that was being deposited.

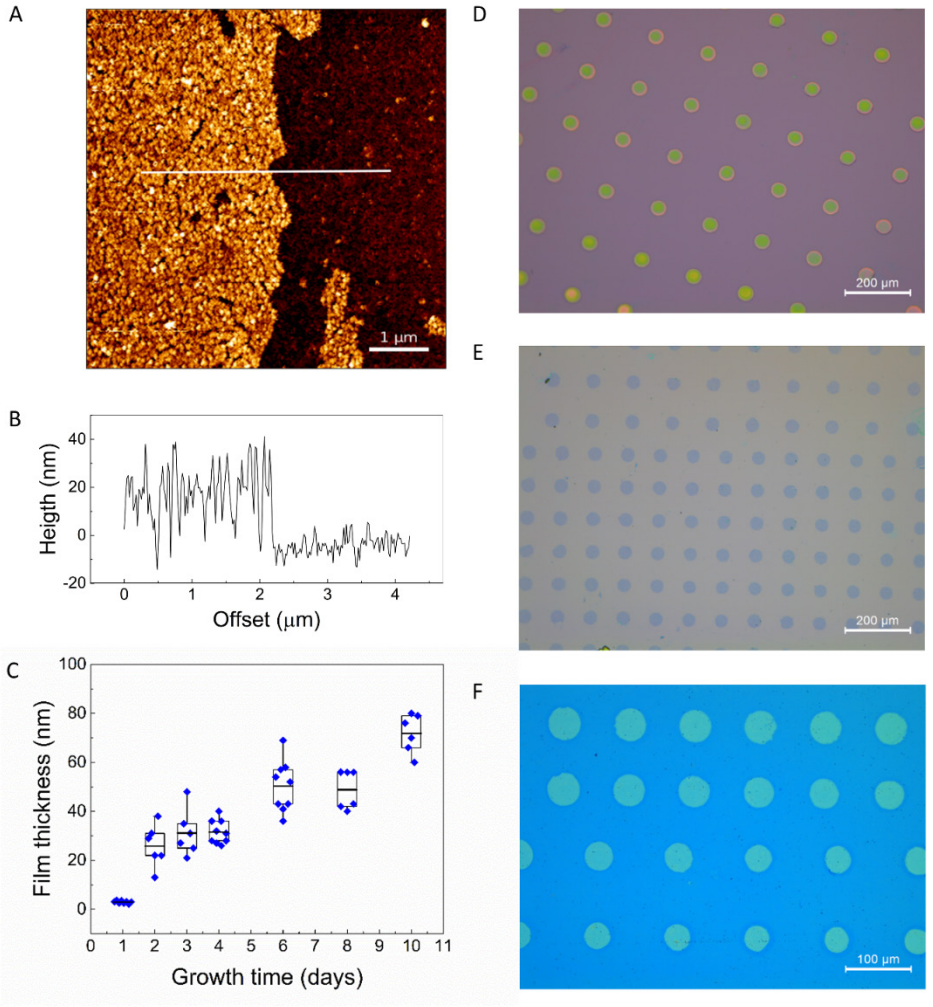

Figure 3.2: **Physical characterization of thin films obtained by vapor diffusion, directly grown on graphene**. A) AFM image of the thin film on large area graphene, growth time for the film was three days. The edge of the film was produced by making a scratch using a razor blade. B) Height profile of a cross section of the thin film shown in A. White line indicates the position of the cross section. C) Box plot of film thickness on large-area graphene as measured by AFM *vs.* growth time. The box represents 25-75% probability, the average is indicated by the horizontal line in the box, and whiskers represent 1- 99% probability. Blue squares are individual measurements. D) Optical image of a PMMA mask printed on graphene on silicon wafer with μ-contact printing. E) Patterned graphene on a silicon wafer, obtained by plasma etching of excess graphene and removing of the polymer mask. F) Thin films grown by vapor diffusion of methanol into a DMF solution of $[Fe(bapbpy)(NCS)_2]$ (15 mM) on patterned graphene after 6 days. Color contrast between graphene coated and non-coated wafer indicates the film grew faster on graphene coated areas, *i.e.* the film grows selectively on graphene.

A quantitative study of the thickness and topology of the films using atomic force microscopy (AFM) showed that already after one day of immersion, the thickness of the hybrid film was ~4 nm, as compared to ~2 nm for a bare graphene sheet, indicating that deposition already started after one day in solution. The thickness of these films was uniform at the micrometer scale (see Figure 3.2A and B). For graphene-coated wafers immersed in the solution of the complex for a longer time (up to ten days), the thickness of the film measured by AFM increased linearly with the growth time (see Figure 3.2C).

When films were grown on wafers that were partially coated with graphene (half of their surface), the thin films had a preference for growing on the graphene-coated area, as compared to the bare wafer surface (SiO_2). In other words, the thickness of the films was typically higher on graphene-coated areas of the wafer. With limited growth time (one to two days immersion in solution), the film in fact grew exclusively on graphene-coated areas, while with increased growth time, the films started to settle on the bare wafer surface as well (see Figure S3.3A-C). The preference of the film to grow on graphene was confirmed by growing films on micro-sized graphene patterns, *i.e.* graphene circles with a few tens of micrometers in diameter. To obtain micro-sized graphene patterns, a polymer solution (PMMA, 6wt% in anisole) was μ-contact printed on a graphene-coated wafer (see Figure 3.1B: I to V and Figure 3.2D). The patterned polymer layer was used as a mask for a subsequent oxygen plasma cleaning step, during which all unmasked graphene was removed. After dissolving the PMMA mask in acetone, the patterned graphene on the wafer surface was exposed to the thin film growth solution (see Figure 3.1B: VI & VII and Figure 3.2E). Thin films formed mainly on the graphene discs, similar to large-area graphene. The film thickness on each disc, but also from disc to disc, was uniform, as seen optically by the light interference effect obtained in presence of the silicon wafer background (see Figure 3.2F, and Figure S3.3D-F for large area images).

3.2.3. Chemical and morphological characterization of the film

The chemical identity of thin films grown by methanol vapor diffusion into a DMF solution of $[Fe(bapbpy)(NSC)_2]$ (grown over multiple days) on graphene was studied using Raman spectroscopy, X-ray diffraction (XRD), energy-dispersive X-ray spectroscopy (EDX), and X-ray photoelectron spectroscopy (XPS). For thicker films, *i.e.* films with a thickness of a few tens of nanometers obtained with film growth times of >5 days, the identity of the film could

unambiguously be assigned to [Fe(bapbpy)(NCS)$_2$], as the Raman peak pattern and relative intensities of the film fitted well with that of the bulk (see Figure 3.3A, for a zoom see Figure S3.4). The Raman signature of thinner films (< 20 nm) also seemed to match in wavenumber with the spectrum of the bulk material, but two major differences were observed. First, the peaks of the thinner films were much broader and hence less resolved than the Raman peaks from thicker films or from the bulk material. Second, the thiocyanate stretching mode at 2100 cm^{-1} in the bulk spectrum was absent. To explain these differences, several control experiments were done.

First, the broadening of the Raman peaks for thinner films of [Fe(bapbpy)(NCS)$_2$] was studied by growing well-identified 3D single crystals of [Fe(bapbpy)(NCS)$_2$] on a wafer, and then intentionally damaging them by sonicating the wafer (immersed in water) for 10 seconds, leaving a thin residue that originated from the crystal on the wafer, the chemical nature of which was hence known. The height of this thin residue was measured with AFM while Raman spectra were recorded at the same location (see Figure S3.5). With decreasing thicknesses of the crystal residue, the Raman peaks in the range of 1100 to 1600 cm^{-1} indeed broadened, starting from the well-resolved spectrum of the bulk material when the film thickness was 20 nanometer or higher, to end up with three broad peaks at 1334, 1429, and 1579 cm^{-1} when the thickness was less than 15 nm. Thin materials of [Fe(bapbpy)(NCS)$_2$] thus show broad peaks in Raman spectroscopy.

Second, Raman spectra of 3D single crystals of [Fe(bapbpy)(NCS)$_2$] grown on wafer were recorded at different orientations with respect to the Raman laser incidence. The relative intensities of several bapbpy-based Raman modes and the stretching mode of thiocyanate were found to vary with the sample rotation angle. The thiocyanate stretching mode even completely disappeared at certain angles (Figure S3.6). This effect, typical for crystalline materials, originates from the relation between the local crystallographic orientation and the polarization of the Raman laser,[14, 15] and was used before to study the local crystallographic orientation in for example silicon crystals and thin films[14, 16], and graphene.[17] For thin films of [Fe(bapbpy)(NCS)$_2$], rotating the wafer did not change the Raman peak intensities, indicating that the thin films were not crystalline, *i.e.* amorphous, which was confirmed by performing X-ray-diffraction (XRD) analysis of thin films of various thickness (see Figure S3.7). Overall, Raman and XRD analysis

strongly suggested that the thin films were composed of [Fe(bapbpy)(NCS)$_2$] molecules arranged in an amorphous film.

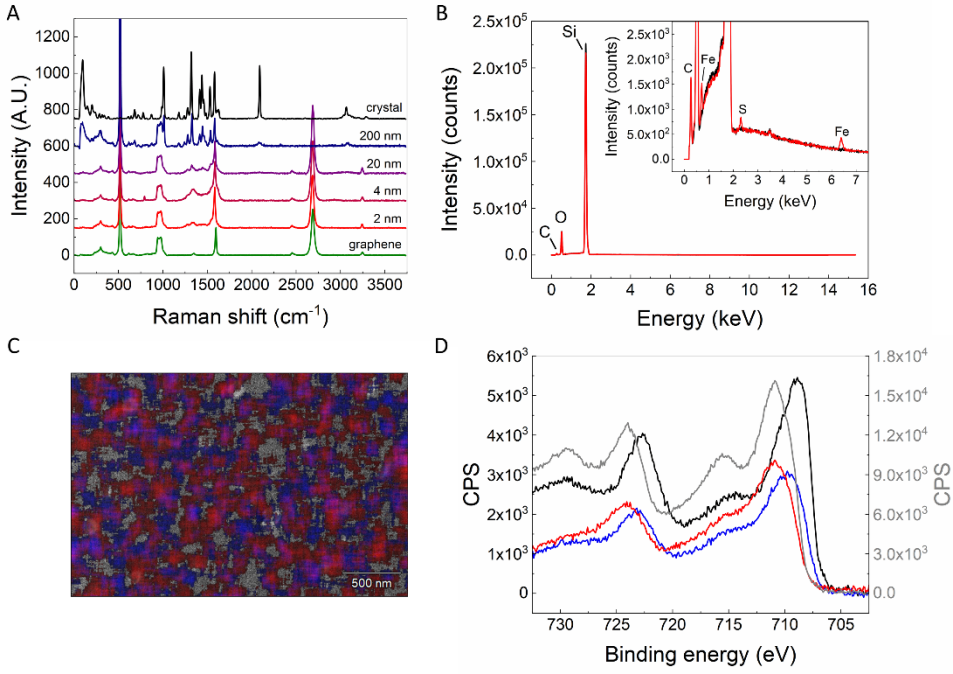

Figure 3.3: Chemical characterization of thin films obtained by vapor diffusion grown on graphene. A) Raman spectrum of bare graphene on silicon wafer (green), graphene coated with thin films of [Fe(bapbpy)(NCS)$_2$] with different thicknesses (red to blue), and single crystals of the HS phase of [Fe(bapbpy)(NCS)$_2$] (black) at room temperature. B) EDX analysis of 20 nm thin film (red) and graphene (black) on silicon wafer. Inset: zoom showing iron and sulfur peaks in the thin film. C) EDX elemental mapping (atomic%) of a 20 nm thin film, overlay of iron (red) and sulfur (blue). D) XPS analysis in Fe 2p peak range of thin films grown under oxygenic conditions (red) and under nitrogen (blue) and of ground [Fe(bapbpy)(NCS)$_2$] crystals (black), all on the left y-axis, and $FeCl_3$ (grey) on the right y-axis. Counts per second (CPS) was set to 0 at 700 eV for all spectra for clarity.

To study the elemental composition of the thin films on graphene we used energy-dispersive X-ray spectroscopy (EDX), which can be used as a qualitative method for element detection in surfaces. The EDX spectra showed small peaks at 0.28, 2.31 and 6.40 keV, characteristic for respectively carbon (C), sulfur (S) and iron (Fe), next to the intense peaks at 0.53 and 1.74 keV for oxygen and silicon from the silicon oxide wafer (see Figure 3.3B). The C, S and Fe peaks were especially more intense for thicker films. The presence of nitrogen (N) in the film could not be confirmed with EDX, as the nitrogen peak at 0.39 keV overlapped with the intense

oxygen peak. The sulfur could hypothetically originate from the etching process of copper with ammonium persulfate, however S (or Fe) was not found in the EDX spectra of control samples made of bare graphene on silicon wafer. Elemental EDX maps showed an even distribution of carbon, iron and sulfur over micrometer-sized areas (see Figure 3.3C and Figure S3.8). Overall, elemental analysis of these thin films by EDX showed that both iron and sulfur originating from the [Fe(bapbpy)$(NCS)_2$] complex were present.

To further assess the chemical composition of the films and notably on the oxidation state of iron (II *vs.* III), we turned to X-ray photoelectron spectroscopy (XPS). XPS is a more powerful analysis technique than EDX, as it not only gives qualitative information about the presence of certain elements, but also has a higher sensitivity, and can provide information about the oxidation state of these elements. First of all, the full XPS spectra of the thin films (20 nm, growth time = 3 days) showed good overlap with the spectrum of the bulk [Fe(bapbpy)$(NCS)_2$] crystals (see Figure S3.9). The Fe 2p peak at 709.8 eV for samples grown under nitrogen atmosphere showed a mixed iron(II)-iron(III) character. While the peak for bulk [Fe(bapbpy)$(NCS)_2$], which is a pure iron(II) species, appeared at 708.9 eV (Figure 3.3D), films that were grown under atmospheric oxygen and hence contained mainly oxidized iron(III) species were characterized by an iron peak at 710.9 eV that was essentially the same as that of $FeCl_3$, which was used as a reference for Fe(III). The shift to higher binding energies of the Fe 2p peak for thin films grown under nitrogen, but not in a glove box, demonstrated that these films were only partially protected from oxygen. Overall, the films grown by methanol vapor diffusion into DMF solution of the complex were amorphous films that were composed by a mixture of [Fe^{II}(bapbpy)$(NCS)_2$] molecules that may show spin-crossover properties, but also of [Fe^{III}(bapbpy)$(NCS)_2]^+$ molecules, for which SCO has never been observed.

3.2.4. Switching behavior of the thin films

Considering that the films were (at least partially) composed of paramagnetic [Fe^{II}(bapbpy)$(NCS)_2$] molecules, we examined the magnetic properties of the thin films, not grown on graphene, but grown on bare silicon wafer (20 nm) to eliminate any additional magnetic contributions due to graphene transfer. The $\chi \cdot T$ product, where χ is the magnetic susceptibility and T the temperature (as the mass of the material was unknown, we could not obtain the molar magnetic susceptibility, $\chi_m \cdot T$) was dominated by the strongly diamagnetic silicon wafer,

which gave a negative constant contribution χ_{dia} to $\chi \cdot T$. Yet after subtracting χ_{dia}, we found that variations in $\chi \cdot T$ occurred in 1 of the 4 measured samples, in both the cooling and heating mode at $T_{1/2}$ = 122 K, with equal absolute magnitude Δ (see Figure 3.4). These variations resembled a semi-gradual spin transition without hysteresis, which is significantly different from the SCO behavior of 3D crystals of [Fe(bapbpy)(NCS)$_2$]. This difference can be attributed to the amorphous nature of the film, which would lower the cooperativity of spin crossover. The differences between the four samples were likely due to ageing of the films before measurement, during which partial aerial oxidation of the thin films could take place. Thus, these results points towards thin films that would be able to perform SCO. Yet, partial oxidation and inconsistencies in the SCO behavior of different thin film samples suggest that film should be grown in an oxygen-free environment and the thin films should be protected from O_2.

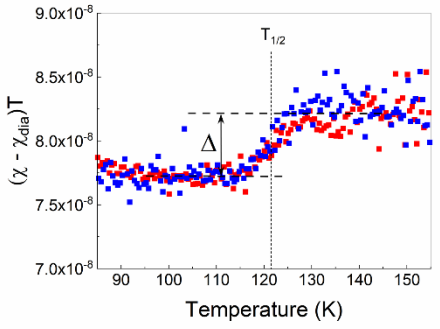

Figure 3.4: SCO behavior of an Fe(bapbpy)(NCS)$_2$-based thin film grown on silicon wafer. Magnetic susceptibility times temperature $\chi \cdot T$ (diamagnetic contribution subtracted) *vs.* temperature of a thin film on silicon wafer (20 nm), measured by SQUID magnetometry, during cooling (blue) and heating (red) mode. The temperature was cycled between 300 and 4 K, at 2 Kmin^{-1}.

3.2.5. Thin film coated device fabrication

We used the preferred growth of films of [Fe(bapbpy)(NCS)$_2$] on graphene-covered areas of the wafer to produce graphene-based GFET devices, to see whether SCO could be electrically sensed by graphene. GFETs were fabricated by transferring graphene over gold electrodes that were deposited on a silicon wafer using gold sputtering (75 nm Au @ 5 nm Cr, Figure 3.5A). We used a 6 parallel electrode configuration: the outside electrodes A & F were used to drive a current through the graphene sheet (to eliminate contact resistance) and the potential was read between the inner electrodes B & C, and D & E, referred to as MEAS(urement) and REF(erence) (Figure 3.5B). The GFETs were coated with the

thin film by using them as the substrate in thin film growing experiments. Again, the film formed preferentially on graphene-coated areas, as observed with the naked eye and with AFM. Importantly, for the GFETs it was essential to limit the film growth time, as the DMF/MeOH solutions that were used to produce the molecular thin film visibly etched the gold electrodes. Yet, when the growth time was <48 h, the electrodes could still be electrically connected with copper wire to produce intact GFETs (for a photograph of a GFET, see Figure S3.10).

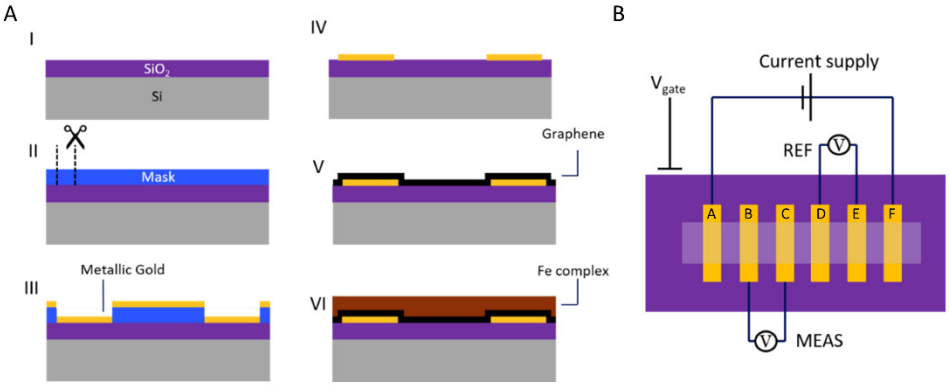

Figure 3.5: GFETs coated with a thin film. A) Schematic representation of fabrication of graphene-PMMA sensors, step by step. A silicon wafer was cleaned (I), coated with a mask with the electrodes cut out (II). A layer of chromium (5 nm), then gold (75 nm) was deposited on the masked wafer (III) and the mask was removed (IV). Next, graphene was transferred over the electrodes (V). Lastly, a thin film of the [Fe(bapbpy)(NCS)$_2$] was grown on the device by methanol vapor diffusion into a DMF solution of the complex (15 mM) over one or two days (VI). B) Schematic top view of typical devices with reference (REF) and measurement (MEAS) transistors. A gate voltage was applied on the back side of the silicon wafer to apply an electric field to the GFET through the SiO_2 layer.

The thin-film coated GFETs were subjected to cooling and heating over a wide temperature range (293 to 138 K). While going through the temperature cycle, the resistance of the graphene sheets coated with the thin film was measured continuously. While SCO was recorded as a resistance variation when 3D single crystals of [Fe(bapbpy)(NCS)$_2$] were interfaced with graphene (see Chapter 2),[7] no resistance variations could be observed upon temperature cycling for the thin film-coated GFETs (see Figure S3.11). In other words, either the thin film had no SCO properties, or they occurred at temperatures outside the tested temperature range, as suggested by the magnetic susceptibility measurements (see Figure 3.4). On the other hand, the effects of such SCO properties on graphene resistance could be too minute to be observed via resistance measurements in this experimental configuration.

For now, it is difficult to distinguish between these three different interpretations. Although the physical-chemical analyses of the films strongly suggests that the thin films were composed of the same molecules as the bulk single crystals of [Fe(bapbpy)(NCS)$_2$], it is not certain how much the presence of oxidized iron(III) centers disturbs the SCO properties of nearby iron(II) molecules. Also, due to technical limitations of our setup, temperatures lower than 138 K could not be reached in the graphene resistance measurements, while according to magnetometry the amorphous thin film seemed to undergo SCO at lower temperatures. Clearly, either iron(III) impurities or amorphousness[2] prevents the film from showing the highly cooperative SCO observed in 3D crystal. Lacking abrupt transitions complicates the detection of SCO by graphene resistance measurements, as the SCO-induced changes in resistance are spread out over a large temperature range, thus leading to small signal-to-noise ratios. This effect is expected to be especially challenging considering the smaller magnitude expected for GFET functionalized with thin films, compared to GFET functionalized with thick bulk single crystals. Overall, the amorphousness of the thin films, and the resulting poor cooperativity of their SCO, appear as major challenges for the detection of SCO via resistance measurements in thin-film functionalized GFET.

3.3. Conclusions & Outlook

Thin films of the complex [Fe(bapbpy)(NCS)$_2$] were produced on graphene-coated silicon wafers on a centimeter scale through a methanol vapor diffusion method. Formation of the thin film was found to be selective for graphene-coated areas of the wafer, as compared to clean silicon wafer, both for large graphene areas and for patterned, micrometer-sized patches of graphene. The thin films on graphene were tunable in thickness ranging from few nanometers to hundreds of nanometers by simply increasing the growth time. A combination of physical and chemical techniques showed that the films have the same molecules, but different morphology and crystal structure as the bulk 3D [Fe(bapbpy)(NCS)$_2$] crystals, and that the iron complex in the film was partly oxidized. Magnetic susceptibility experiments hinted on the existence of spin crossover in the thin films, albeit at lower temperatures and with less cooperativity than in the bulk. Reproduction will be required to confirm this, if possible with the samples strictly protected from molecular oxygen. When these thin films were grown on graphene field effect transistors, their SCO behavior could not be detected by electrical resistance measurements, as has been reported in Chapter 2 for bulk single crystals of

[Fe(bapbpy)(NCS)$_2$]. We believe that, to allow detection, the cooperativity and oxidation state of the bulk material should be retained in the films. Finally, this work contributes to the field by presenting a method to produce large-area molecular thin films that form with a high preference onto graphene.

3.4. Acknowledgements

We kindly acknowledge Dr. W. Noorduin for supplying μ-contact printing stamps and for scientific discussions. Ted de Haas and Reinout Ubbink are thanked for experimental contributions and scientific discussion.

3.5. References and Notes

[1] D. W. Bruce, D. O'Hare, R. I. Walton, *Molecular Materials*, John Wiley & Sons, Ltd., **2011**; O. Kahn, C. J. Martinez, *Science* **1998**, *279*, 44.
[2] P. Gütlich, A. B. Gaspar, Y. Garcia, *Beilstein J. Org. Chem.* **2013**, *9*, 342.
[3] J. A. Real, A. B. Gaspar, M. C. Munoz, *Dalton Trans.* **2005**, *0*, 2062.
[4] G. Molnár, S. Rat, L. Salmon, W. Nicolazzi, A. Bousseksou, *Adv. Mater.* **2018**, *30*, 1703862; C. Lefter, V. Davesne, L. Salmon, G. Molnár, P. Demont, A. Rotaru, A. Bousseksou, *Magnetochemistry* **2016**, *2*, 18.
[5] K. Senthil Kumar, M. Ruben, *Coord. Chem. Rev.* **2017**, *346*, 176; M. A. Halcrow, *Chem. Lett.* **2014**, *43*, 1178; O. Roubeau, *Chem. Eur. J.* **2012**, *18*, 15230; A. Bousseksou, G. Molnar, L. Salmon, W. Nicolazzi, *Chem. Soc. Rev.* **2011**, *40*, 3313.
[6] Y. Raza, F. Volatron, S. Moldovan, O. Ersen, V. Huc, C. Martini, F. Brisset, A. Gloter, O. Stéphan, A. Bousseksou, L. Catala, T. Mallah, *Chem. Commun.* **2011**, *47*, 11501.
[7] E. P. van Geest, K. Shakouri, W. Fu, V. Robert, V. Tudor, S. Bonnet, G. F. Schneider, *Adv. Mater.* **2020**, *32*, 1903575.
[8] T. G. Gopakumar, F. Matino, H. Naggert, A. Bannwarth, F. Tuczek, R. Berndt, *Angew. Chem., Int. Ed.* **2012**, *51*, 6262.
[9] S. Bonnet, G. Molnár, J. Sanchez Costa, M. A. Siegler, A. L. Spek, A. Bousseksou, W.-T. Fu, P. Gamez, J. Reedijk, *Chem. Mater.* **2009**, *21*, 1123.
[10] C. N. Kaplan, W. L. Noorduin, L. Li, R. Sadza, L. Folkertsma, J. Aizenberg, L. Mahadevan, *Science* **2017**, *355*, 1395; J. Aizenberg, D. A. Muller, J. L. Grazul, D. R. Hamann, *Science* **2003**, *299*, 1205.
[11] W. Fu, L. Jiang, E. P. van Geest, L. M. C. Lima, G. F. Schneider, *Adv. Mater.* **2017**, *29*, 1603610.
[12] M. Kepenekian, J. S. Costa, B. Le Guennic, P. Maldivi, S. Bonnet, J. Reedijk, P. Gamez, V. Robert, *Inorg. Chem.* **2010**, *49*, 11057.
[13] S. Bonnet, M. A. Siegler, J. S. Costa, G. Molnar, A. Bousseksou, A. L. Spek, P. Gamez, J. Reedijk, *Chem. Commun.* **2008**, *0*, 5619.
[14] J. B. Hopkins, L. A. Farrow, *J. Appl. Phys.* **1986**, *59*, 1103.
[15] Q. Song, X. Pan, H. Wang, K. Zhang, Q. Tan, P. Li, Y. Wan, Y. Wang, X. Xu, M. Lin, X. Wan, F. Song, L. Dai, *Sci. Rep.* **2016**, *6*, 29254.
[16] K. Mizoguchi, S. i. Nakashima, *J. Appl. Phys.* **1989**, *65*, 2583; Z. Q. Lu, T. Quinn, H. S. Reehal, *J. Appl. Phys.* **2005**, *97*, 033512.
[17] M. Huang, H. Yan, C. Chen, D. Song, T. F. Heinz, J. Hone, *Proc. Natl. Acad. Sci.* **2009**, *106*, 7304.